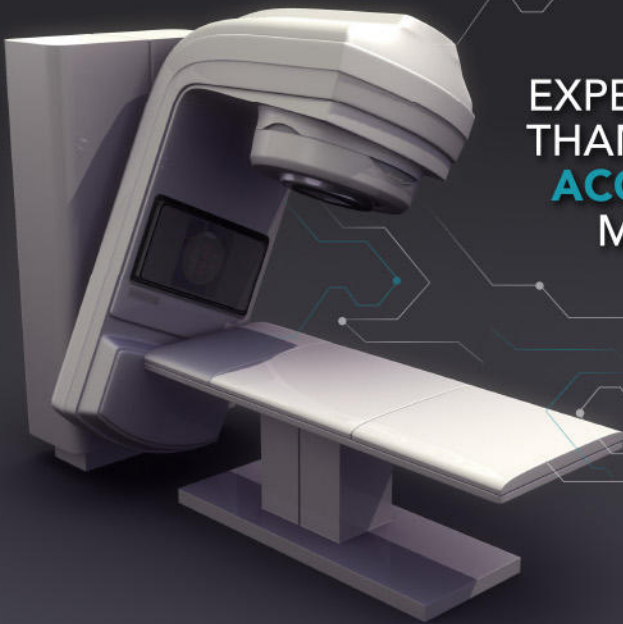




EXPECT NOTHING LESS THAN **SUB-MILLIMETER ACCURACY** IN YOUR MEASUREMENTS



START UTILIZING ADVANCED PRECISION QA TODAY

THE RIT FAMILY OF PRODUCTS **VERSION 6.7.X**

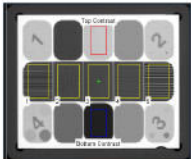
3D Winston-Lutz Isocenter Optimization

The enhanced isocenter optimization routine allows for optimal cone detection, resulting in the utmost precision. The accuracy of this routine now surpasses sub-millimeter resolution. *(Pictured above)*

Cerberus 2.0: The Future of Complete Automation

Completely streamline your automated phantom analysis workflow with the new Cerberus. Cerberus operates in the background of your workstation, allowing for hands-free Imaging QA.

One-Click, Instant Automated Phantom Analyses



RIT's full suite of phantom analyses provides fast, robust, and accurate analysis of all imaging tests recommended in TG-142. The software now offers added support for the QcKv-1 phantom. *(Pictured right)*

Tolerance Customization and Management

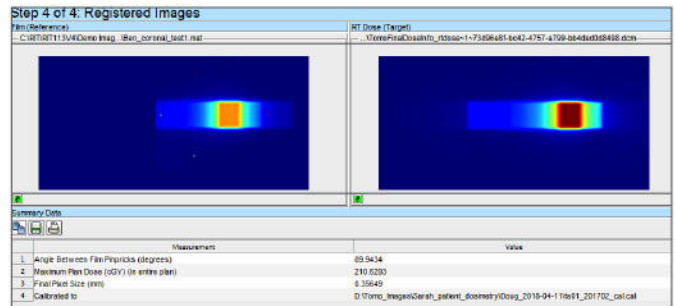
RIT's new Tolerance Manager offers comprehensive customization of tolerance values for every measurement used in all automated phantom analyses. Tolerance profiles can be precisely-tailored to each individual machine in use.

Elekta Leaf Speed Analysis

RIT now offers fast and accurate automated analysis for Elekta MLC QA. The new Leaf Speed Analysis routine measures the consistency and accuracy of the MLC leaf speeds as they traverse the imager.

TomoTherapy® Registration for Patient QA

Easily perform exact dose comparisons with RIT's new TomoTherapy Registration routine. This new, innovative wizard uses a TomoTherapy® plan, dose map, and a film to determine position and dose accuracy using the red lasers. *(Pictured below)*



Streamline Your QA Workflow

Fully-customize your software experience with RIT's updated and dynamic interface. With the new ability to hide/display any features or sections, you can instantly access you most frequently-performed analysis routines.

Convenient, Cloud-Based Software Licensing

Easily manage your software licenses with RIT's new, flexible system at your convenience, 24/7/365 without the help of RIT Technical Support. Upgrading is now easier than ever.

CLICK HERE TO DOWNLOAD TODAY

RADIOLOGICAL IMAGING TECHNOLOGY, INC.

RADIMAGE.COM

(+1) 719.590.1077 x211 // sales@radimage.com

Connect with RIT
@RIT4QA



©2018, Radiological Imaging Technology, Inc.
TomoTherapy® is a registered trademark of Accuray, Inc.

Proof-of-concept prototype time-of-flight PET system based on high-quantum-efficiency multianode PMTs

Jeong-Whan Son and Kyeong Yun Kim

Department of Biomedical Sciences, Seoul National University College of Medicine, Seoul 03080, Korea
Department of Nuclear Medicine, Seoul National University College of Medicine, Seoul 03080, Korea

Hyun Suk Yoon

Department of Nuclear Medicine, Seoul National University College of Medicine, Seoul 03080, Korea

Jun Yeon Won and Guen Bae Ko

Department of Biomedical Sciences, Seoul National University College of Medicine, Seoul 03080, Korea
Department of Nuclear Medicine, Seoul National University College of Medicine, Seoul 03080, Korea

Min Sun Lee

Department of Nuclear Medicine, Seoul National University College of Medicine, Seoul 03080, Korea
Interdisciplinary Program in Radiation Applied Life Science, Seoul National University, Seoul 03080, Korea

Jae Sung Lee^{a)}

Department of Biomedical Sciences, Seoul National University College of Medicine, Seoul 03080, Korea
Department of Nuclear Medicine, Seoul National University College of Medicine, Seoul 03080, Korea
Interdisciplinary Program in Radiation Applied Life Science, Seoul National University, Seoul 03080, Korea
Institute of Radiation Medicine, Medical Research Center, Seoul National University College of Medicine, Seoul 03080, Korea

(Received 3 March 2017; revised 21 June 2017; accepted for publication 22 June 2017; published 18 August 2017)

Purpose: Time-of-flight (TOF) information in positron emission tomography (PET) scanners enhances the diagnostic power of PET scans owing to the increased signal-to-noise ratio of reconstructed images. There are numerous additional benefits of TOF reconstruction, including the simultaneous estimation of activity and attenuation distributions from emission data only. Exploring further TOF gains by using TOF PET scanners is important because it can broaden the applications of PET scans and expand our understanding of TOF techniques. Herein, we present a prototype TOF PET scanner with fine-time performance that can experimentally demonstrate the benefits of TOF information.

Methods: A single-ring PET system with a coincidence resolving time of 360 ps and a spatial resolution of 3.1/2.2 mm (filtered backprojection/ordered-subset expectation maximization) was developed. The scanner was based on advanced high-quantum-efficiency (high-QE) multianode photomultiplier tubes (PMTs). The impact of its fine-time performance was demonstrated by evaluating body phantom images reconstructed with and without TOF information. Moreover, the feasibility of the scanner as an experimental validator of TOF gains was verified by investigating the improvement of images under various conditions, such as the use of joint estimation algorithms of activity and attenuation, erroneous data correction factors (e.g., without normalization correction), and incompletely sampled data.

Results: The prototype scanner showed excellent performance, producing improved phantom images, when TOF information was employed in the reconstruction process. In addition, investigation of the TOF benefits using the phantom data in different conditions verified the usefulness of the developed system for demonstrating the practical effects of TOF reconstruction.

Conclusions: We developed a prototype TOF PET scanner with good performance and a fine-timing resolution based on advanced high-QE multianode PMTs and demonstrated its feasibility as an experimental validator of TOF gains, suggesting its usefulness for investigating new applications of PET scans and clarifying TOF techniques in detail. © 2017 American Association of Physicists in Medicine [https://doi.org/10.1002/mp.12440]

Key words: PET instrumentation, photomultiplier tubes, time-of-flight PET

1. INTRODUCTION

Time-of-flight (TOF) positron emission tomography (PET) scanners provide reconstructed PET images with a higher signal-to-noise ratio than non-TOF PET, which can lead to

enhanced diagnostic power and/or a reduced scan time or a reduced patient radiation dose.^{1–4} The TOF information also improves the consistency in image reconstruction, making the reconstructed emission data less sensitive to inconsistencies between the emission data and corrections (e.g.,

mismatched attenuation correction and erroneous normalization).⁵ In addition, the robustness of TOF PET to incomplete angular sampling has been demonstrated through several simulation studies (e.g., dedicated breast PET and in-beam PET).^{5–7} Another remarkable benefit of TOF PET is the improved simultaneous estimation of activity and attenuation distributions from only the emission data via joint reconstruction algorithms.^{8,9} This approach is particularly important in PET scanners that suffer from limited information about the attenuation distributions (e.g., PET/magnetic resonance imaging (MRI) systems).

In the conventional TOF PET detectors, scintillation light generated from a rectangular array of long and narrow crystals (e.g., $4 \times 4 \times 20 \text{ mm}^3$) is read out by multiple single-channel PMTs (e.g., block detectors and quadrant-sharing methods).^{10–12} Although the detector costs can be reduced by using single-channel PMTs, the time performance of the PET detector is significantly compromised in this light-sharing scheme because of the increased light loss and transit-time jitter. Recently, alternative TOF PET detector structures based on advanced photosensor technologies have become available. Such advanced photosensors include the silicon photomultiplier (SiPM) and the high-quantum-efficiency (high-QE) multianode PMT. The compactness of the SiPMs enables the 1-to-1 coupling of a crystal piece with each SiPM device, improving the light collection and time performance.^{13–15} MRI compatibility is another advantage of this new solid-state photosensor.^{16–18} On the other hand, the position-sensitive multianode PMT is based on well-proven vacuum-tube technology, offering highly stable PET detector operation that is less prone to fluctuations in the supply voltage and detector temperature than the operation of the SiPM. The relatively low dark count noise¹⁹ and output capacitance compared with the SiPM allow a higher ratio of signal multiplexing, reducing the number of output signal channels from PET detectors. Radiation hardness is another benefit of PMT-based PET systems, which is important for real-time in-beam monitoring of β^+ activity distributions generated by charged-hadron irradiation for radiation therapy.

Herein, we present a prototype whole-body TOF PET scanner based on high-QE multi-anode PMTs with a superbiaikali photocathode, a small pixel size, a large effective

area, a high packing density, and excellent time performance (360 ps coincidence timing resolution). To obtain a high spatial resolution, we used Lu-based scintillators with smaller cross-sections (3 mm) than those of crystals widely used in current clinical scanners (4 mm). Higher spatial resolution (3.1 mm) is the advantage of our system over the single-channel PMT-based PET scanners with similar timing resolutions [i.e., 314 ps²⁰ (5.1 mm) and 375 ps²¹ (5.8 mm)]. The detailed system design and performance-evaluation results are presented. Additionally, various phantom studies were performed to show the feasibility of the proposed PET system as an experimental demonstrator of the benefits of precise TOF measurement (i.e., image quality enhancement, robustness to inconsistent and incomplete data, and joint activity/attenuation estimation) under more clinically relevant condition compared to the above-mentioned PET scanners with similar timing resolutions (i.e., longer axial coverage (46.4 mm vs. 6.15 mm²⁰) and practical scintillator selection (LGSO vs. LaBr₃²¹)).

2. MATERIALS AND METHODS

2.A. Prototype TOF PET scanner

The prototype TOF PET system is comprised of forty detector modules—each consisting of a 15×15 array of LGSO ($\text{Lu}_{1.9}\text{Gd}_{0.1}\text{SiO}_4\text{:Ce}$, Hitachi Chemical Co., Tokyo, Japan) crystals ($3 \times 3 \times 20 \text{ mm}^3$) and an advanced high-QE (34.1%@420 nm) position-sensitive multianode PMT (H10966A-100, Hamamatsu Photonics K. K., Hamamatsu, Japan) [Fig. 1]. The H10966A-100 PMT has considerably higher quantum-efficiency than H8500 PMT, the most widely used conventional 64-channel multianode PMT with 24% QE. High-QE of a PMT yields improved crystal identification ability, energy resolution, and timing resolution thanks to the reduced statistical uncertainties, which resulted from the higher number of photoelectrons generated.^{22–24} The crystals are isolated from each other by enhanced specular reflectors ($> 98\%$ reflectance, 0.065-mm thickness; 3 M), and the pitch was 3.1 mm. The diameter of the scanner is 64.1 cm, and the gaps between adjacent detector modules are smaller than two crystals. The main characteristics of the PET scanner are

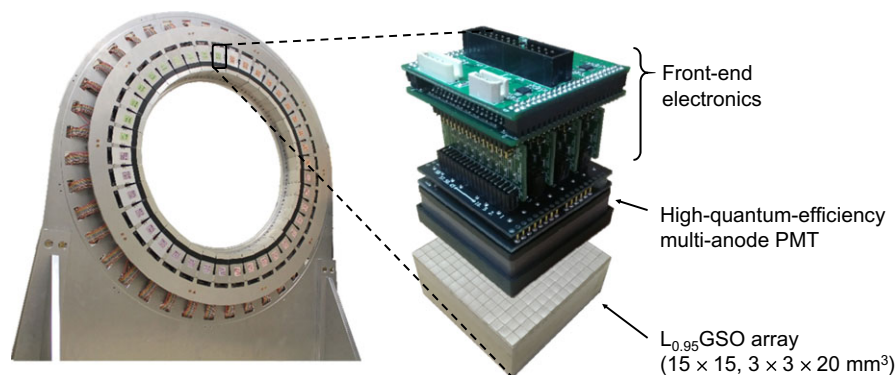


FIG. 1. Developed TOF PET scanner and its detector module. [Color figure can be viewed at wileyonlinelibrary.com]

summarized in Table I. The energy and coincidence time windows used in the performance measurements and phantom studies were 435–590 keV and 4 ns respectively. Analog electronics, including a gain-compensation circuit,²⁵ a charge-division network,²⁶ and a bipolar multiplexer,²⁷ were developed. A field-programmable gate array-based time-to-digital converter (12.8 ps measurement uncertainty, 200 MSa/s maximum conversion rate)²⁸ and a data-acquisition system (6.8 Mc/s maximum count rate)²⁹ were also employed. The detailed detector design and data-acquisition setup of the PET scanner as well as the effect of high-QE on detector performance are described in another study.³⁰

2.B. System performance measurement

The system-level energy, timing, and spatial resolutions were measured using a ²²Na point source (MMS06-022, Eckert & Ziegler, Berlin, Germany) located at the center of the scanner and coincidence data were acquired. In the flood map of each detector, the distance-to-width ratio (DWR) was calculated as the figure of merit of the pixel coding efficiency of the scanner.³¹ The average DWR of a PET detector consisting of $N \times M$ crystals is calculated using the following equation (i and j are adjacent):

$$\text{DWR}_{\text{avg}} = \frac{1}{2NM - N - M} \sum_{(i,j) \in (\text{adj pair})} \frac{\text{distance}(\text{crystal}_i, \text{crystal}_j)}{(\text{FWHM}_i + \text{FWHM}_j)/2}$$

The energy resolution was calculated as the full width at half maximum (FWHM) of a Gaussian function fitted to the 511-keV photopeak normalized by the peak. The timing resolution was calculated as the FWHM of a Gaussian function fitted to the histogram of the arrival-time differences. The spatial resolution of the scanner was measured using a ²²Na point source positioned at the center of the axial FOV and 1 and 10 cm away from the center in the transverse FOV respectively. Two images were reconstructed using different algorithms: the two-dimensional filtered back-projection (2D FBP) algorithm and the three-dimensional ordered-subset expectation maximization (3D OSEM) algorithm (1 iteration and 15 subsets). The image matrix size of the reconstructed images was $512 \times 512 \times 29$, with a voxel size of

TABLE I. Main characteristics of the high-QE multianode PMT-based prototype TOF PET scanner.

Characteristics	Value
Crystal material	L _{0.95} GSO
Crystal dimension (mm ³)	$3 \times 3 \times 20$
# crystal rings	15
# crystals/ring	600
Total # crystals	9000
Transaxial FOV (mm)	518
Axial FOV (mm)	46.4

$0.8 \times 0.8 \times 1.55 \text{ mm}^3$. Single-slice rebinning was applied before the 2D FBP reconstruction. The spatial resolutions [FWHM and full width at tenth maximum (FWTM)] were calculated using a method specified in NU2-2007 by the National Electrical Manufacturers Association (NEMA).³² Sensitivity and count-rate performance of the prototype scanner were also measured although limited results were expected because of its short axial length. The measurement and analysis were done following the NEMA NU2-2007 protocol.³²

2.C. Image quality measurement

The NEMA International Electrotechnical Commission (IEC) body phantom was scanned to evaluate the improved PET image quality, owing to the excellent time performance of the prototype scanner. The background activity of the phantom filled with a ¹⁸F solution was 5.3 kBq/cc, and the concentration ratio of the hot lesions to the background was 4:1. A total of 48 million coincidence events were acquired.

Data were stored in a list-mode format. Images were reconstructed using a 3D list-mode OSEM algorithm with and without TOF modeling. The parameters for both TOF and non-TOF reconstructions were as follows: 15 subsets, 5 iterations, a 5-mm (FWHM) transaxial postfilter, and a 3-mm axial post-filter. While fixing the number of subsets, the optimal number of iterations was determined to five at which contrast of the image was converged. The image matrix was $128 \times 128 \times 29$ in size, with a voxel size of $3.1 \times 3.1 \times 1.55 \text{ mm}^3$. Attenuation correction was performed using a registered computed-tomography (CT) image taken from a commercial PET/CT scanner (Biograph mCT 64, Siemens Medical Solutions, Knoxville, TN, USA). Component-based normalization was performed using factors derived from data acquired via a ⁶⁸Ge quality-control phantom (EG-0318-2.5M, Eckert & Ziegler). Random events were estimated from singles rate. The distribution of scatter events was estimated using GATE Monte Carlo simulations, and the tail parts of simulated and measured sinograms were fitted for count scaling that was necessary due to the incompleteness of scatter estimation.

As image quality parameters, the contrast recovery coefficient (CRC) and background variability (BV) for each sphere size were calculated according to the NEMA NU 2-2007 protocol³² except the fact that the background regions-of-interest were drawn at the central slice and ± 1 and ± 1.5 cm away from the central slice. In addition, lung residual error was measured.

2.D. Robustness to errors in data correction

To assess the robustness of the developed TOF PET system to data correction errors, the activity images of the NEMA IEC body phantom were reconstructed without applying one of the attenuation, scatter, and normalization corrections. In addition, we applied attenuation correction with an attenuation map that was intentionally shifted by 10 mm in

the radial direction for investigating the effects of a mismatched attenuation map due to the patient breath or movement. The amount of shift was determined to 10 mm as the average movement of organs such as lung, liver, diaphragm, and pancreas was about 10 mm.³³ The images reconstructed with and without TOF information were compared.

2.E. Partial ring geometry and limited angle tomography

We examined the image quality improvement caused by the TOF reconstruction in the case where our TOF PET system was modified for limited angle tomography with a partial ring geometry by excluding certain detector data from the list-mode data. We tested two different partial ring geometries. The first was the split-ring geometry, which was suggested for scanning the breast with a variable distance between two C-shaped partial rings.^{7,34} This split-ring geometry is also useful for combining the PET system with hadron-therapy instruments^{35,36} and other imaging systems.³⁷ The second is the sparse-ring geometry, in which some of the detectors are intentionally removed to reduce the scanner cost or extend the axial FOV without increasing the cost. Here, detectors were regularly removed to maximize the gap artifacts in reconstructed images due to the incomplete data sampling.

In the split-ring geometry, the gap between two C-shaped partial rings was wide enough (i.e., 140 mm which was the same as used in another study³⁶) for a beam delivery system to be located in the scanner if 10 detectors (i.e., 25%) were removed from the PET scanner. Therefore, 75% of detectors were used in both geometries. The images reconstructed from these incompletely sampled data were compared with an image acquired using the full ring geometry. To compare the amount of artifacts in the background region, a metric [i.e., background uniformity (BU)] was defined as the standard deviation divided by the mean of background pixel intensities because BV cannot reflect overall background artifacts.

2.F. Joint estimation of activity and attenuation

To demonstrate the enhanced performance of the joint activity and attenuation estimation by our PET system with a timing resolution of 360 ps, the IEC body phantom data were reconstructed using common joint estimation algorithms with and without TOF information. One of these algorithms is the maximum-likelihood activity and attenuation estimation (MLAA), in which the maximum-likelihood expectation maximization and maximum-likelihood transmission tomography equations are alternatively applied to update activity and attenuation images.⁸ In each iteration, constant scaling was determined by using a prior on zero attenuation values outside the object contours. The other algorithm tested was the maximum-likelihood attenuation correction factor (MLACF), which determines the attenuation correction factor without reconstruction of the attenuation map for achieving a

fast convergence rate with a lower computation complexity than MLAA.⁹ To determine the constant scaling, the known total activity prior was used in applying the MLACF. The numbers of subsets and iterations were 15 and 5, respectively, in both the MLAA and MLACF. The ratio of subiterations for the activity and attenuation updates was 1:1 in both algorithms. It is worth noting that scatter was estimated using the GATE Monte Carlo simulation, which is not available in real situation. We assumed other factors including scatter were properly corrected in order to solely investigate the effect of 360 ps timing resolution on the performance of joint estimation algorithms.

2.G. Comparison to conventional 600-ps TOF PET

To demonstrate the improvement from 360 ps timing resolution of our PET scanner compared to the conventional 600 ps timing resolution, we compared the images reconstructed using the same data used in Sections 2.D–2.F with different timing resolutions. The timing resolution was degraded to 600 ps by adding Gaussian noise to the timestamps of measured list-mode data.

3. RESULTS

3.A. System performance measurement

The average DWR of the 40 flood maps was 3.8 ± 0.7 , and the representative flood maps are shown in Fig. 2. The average energy resolution was $13.67 \pm 1.48\%$, and the average coincidence resolving time was 360 ± 26 ps. The histograms of the energy and timing resolutions are shown in Fig. 3.

The transverse spatial resolutions near the center of the scanner (1 cm off-center) were 3.5 mm with the FBP algorithm and 2.0 mm with the 3D OSEM algorithm. At 10 cm off-center, the average transverse FWHMs were 4.1 mm (FBP) and 2.7 mm (OSEM). Table II summarizes the transverse and axial spatial resolutions acquired by applying the reconstruction algorithms.

The sensitivity of the scanner was 385 cps/MBq at the center and 404 cps/MBq at a 10 cm radial offset from the FOV center. The peak noise equivalent count rate was 838 cps at 2.31 kBq/ml activity concentration within a scatter phantom. The peak true count rate was 1430 cps at 2.97 kBq/ml activity concentration. The results were shown in Fig. 4.

3.B. Image quality measurement

The images of the IEC body phantom reconstructed with and without TOF information (hereinafter TOF and non-TOF, respectively) and horizontal profiles across the center of the phantom are shown in Fig. 5(a). The solid and dashed lines in the figure correspond to TOF and non-TOF data respectively. The TOF data showed better background uniformity

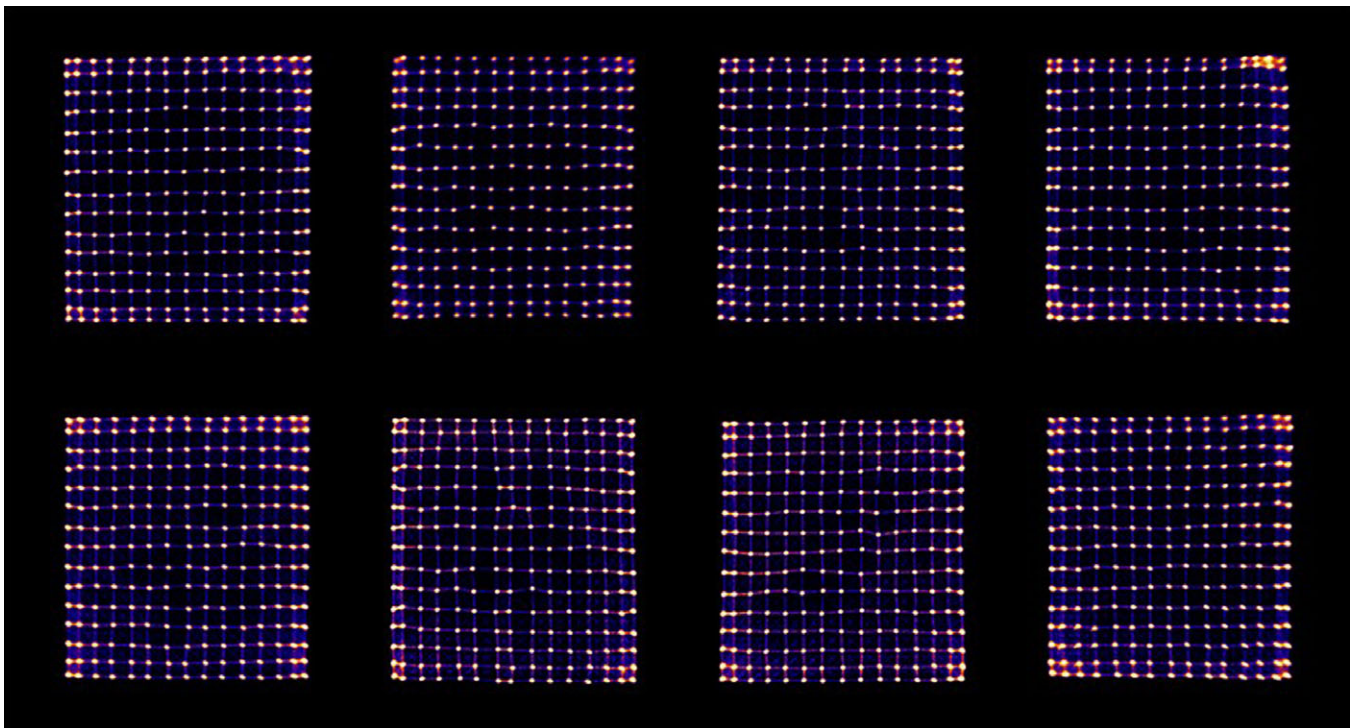


FIG. 2. Representative flood maps of the advanced PMT-based PET scanner. [Color figure can be viewed at wileyonlinelibrary.com]

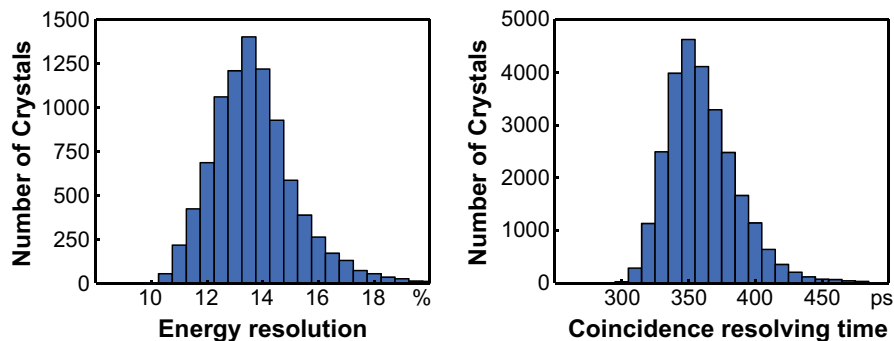


FIG. 3. Histograms of energy resolutions and coincidence resolving times. [Color figure can be viewed at wileyonlinelibrary.com]

TABLE II. Spatial resolution of the scanner.

	Radial position: r = 1 cm		Radial position: r = 10 cm		
	Transverse	Axial	Tangential	Radial	Axial
2D FBP					
FWHM (mm)	3.5	2.7	3.7	4.5	3.9
FWTM (mm)	7.9	6.1	7.7	8.8	6.7
3D OSEM					
FWHM (mm)	2.0	2.4	2.3	3.2	3.1
FWTM (mm)	4.4	5.2	4.7	6.2	6.3

and less artifacts than the non-TOF data. The quantitative measures of image quality (CRCs and BVs) are shown in Figs. 5(b) and 6. The CRCs of the hot lesions were similar between the TOF and the non-TOF images. However, the

CRCs of the cold lesions in the TOF image were higher than those in the non-TOF image. In all spheres, the TOF image showed lower BVs than the non-TOF image. The lung residual errors were $9.2 \pm 0.7\%$ and $14.8 \pm 2.4\%$ in the TOF and non-TOF images respectively.

3.C. Robustness to errors in data correction

The robustness to the errors in data correction achieved by the excellent timing resolution of our TOF PET scanner was well-demonstrated. Figure 7 shows TOF (360 ps), TOF (600 ps), and non-TOF PET images reconstructed without proper physical corrections. In Fig. 7(a), where the images were not corrected for attenuation, the TOF (360 ps) image showed strong robustness to the attenuation artifacts; the background activity near the center of the phantom (between the cold lung insert at the center and the spheres around it)

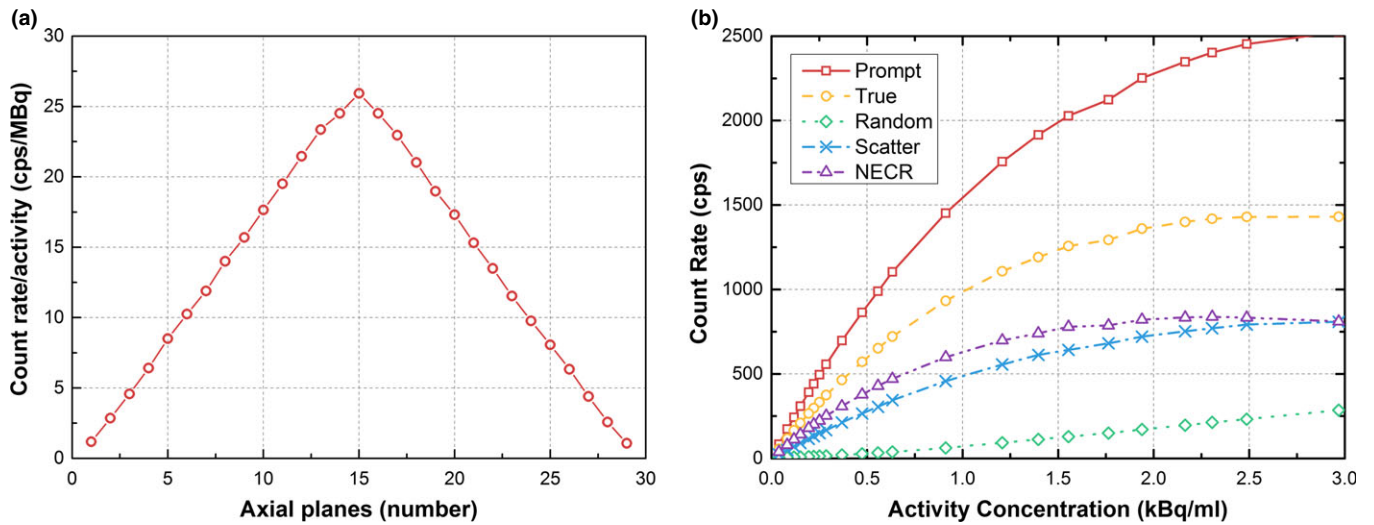


FIG. 4. (a) Axial sensitivity profile and (b) count rates as a function of the activity concentrations within the NEMA scatter phantom. [Color figure can be viewed at wileyonlinelibrary.com]

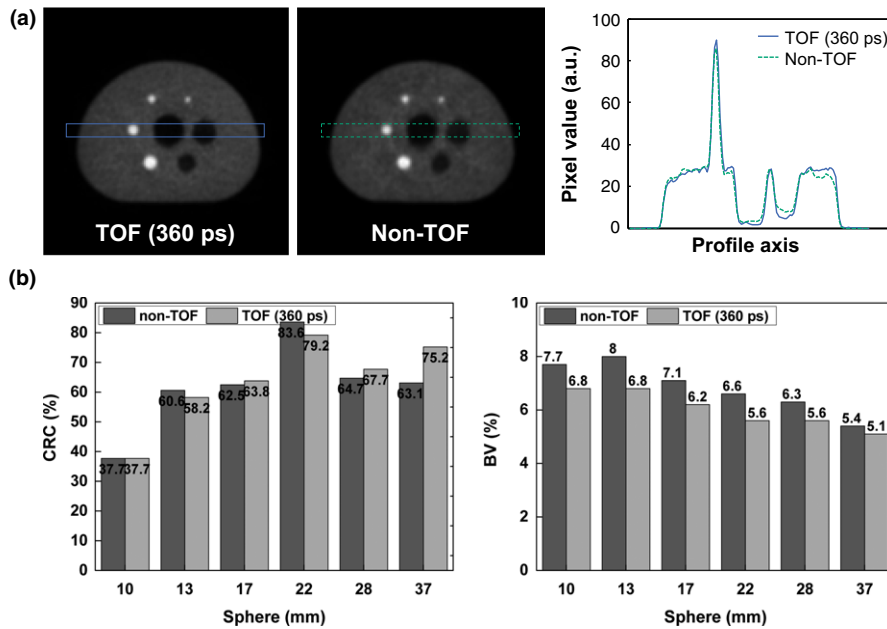


FIG. 5. (a) Phantom images reconstructed with and without TOF information (left) and their horizontal profiles across the center of the phantom (right). (b) CRC and BV values for each sphere of the phantom. [Color figure can be viewed at wileyonlinelibrary.com]

was only slightly lower than that between the spheres and the phantom wall. In contrast, the non-TOF image showed a typical attenuation artifact pattern (i.e., exaggerated activity at the surface and in the lung and severe depth-dependent activity underestimation). In the lung insert, the estimated activity concentration was three times higher in the non-TOF image than in the TOF image. The image artifact due to the mismatch between the activity distribution and the attenuation map is shown in Fig. 7(b). The activity overestimation in a region of interest [the region indicated by arrows in Fig. 7(b)] on the artifact was 42% lower in the TOF image.

Figure 7(c) shows that the increased activity around the center of the phantom and the reduced contrast at the cold lesions observed in the non-TOF image were

considerably mitigated in the TOF image. Severe circular saw-tooth artifacts are observed in the non-TOF image without normalization correction [Fig. 7(d)]. However, these artifacts almost completely disappeared in the TOF image.

Reconstructed images using 600 ps timing resolution showed better robustness to the errors in data correction factors compared to non-TOF images. However, the image artifacts shown in non-TOF images [e.g., higher estimated activity concentration in the lung insert Fig. 7(a) and severe circular saw-tooth patterns Fig. 7(d)] were better mitigated in 360-ps TOF images rather than the 600-ps TOF images, which demonstrated the improvement achieved from about 350 ps timing resolution.

3.D. Partial ring geometry and limited angle tomography

The excellent timing resolution of our TOF PET scanner was also useful for reducing the gap artifacts in the virtual PET systems with a partial ring geometry. Figure 8(a) shows the partial ring geometry (left: split-ring geometry, right: sparse-ring geometry) and Figs. 8(b) and 8(c) show PET images reconstructed from corresponding geometries. For both the partial ring geometries, the images reconstructed with TOF information showed remarkably smaller artifacts near the center of the phantom compared with those reconstructed without TOF information. There was slight improvement in image quality when we compared 360-ps TOF images to 600-ps. Regarding background artifacts of the images, the sparse-ring geometry with TOF (360 ps) yielded comparable BU (i.e., 12.5) with that of the full-ring geometry without TOF (i.e., 11.2). However, in the split-ring geometry, BU was even worse with 360 ps TOF information (i.e., 21.0) compared to the case without TOF (i.e., 16.9) because of the truncation of the left and right sides of the body phantom.

3.E. Joint estimation of activity and attenuation

The accuracy improvement of the joint activity and attenuation estimation using 360 ps TOF information was remarkable, as shown in Fig. 9. Figures 9(a) and 9(b) show the results of joint estimation using MLAA and MLACF respectively. The activity distribution reconstructed using the joint estimation algorithms with TOF information was almost comparable to the activity PET image corrected for attenuation using CT data and reconstructed using the OSEM algorithm. In the jointly estimated activity distribution, the noise level was slightly higher, and the activity on the right side of the phantom was relatively overestimated. The attenuation image estimated using the MLAA algorithm with TOF

information exhibits far smaller crosstalk at the lung insert and hot and cold spheres of the phantom [Fig. 9(a)]. In the case of MLACF algorithm, the reasonable activity distribution was obtained only with the TOF information [Fig. 9(b)].

Compared to 600-ps TOF images, the 360-ps images showed lower estimated activity concentration in the lung region and smaller crosstalk at the spheres of the phantom [Fig. 9(a)]. The 360 ps image reconstructed using the MLACF algorithm showed lower noise level and lower estimated activity concentrations in the cold spheres than those of the 600-ps image [Fig. 9(b)].

4. DISCUSSION

In this study, we developed an advanced high-QE multianode PMT-based prototype TOF PET scanner and measured the performance of the scanner with a focus on the coincidence resolving time, energy, and spatial resolution—360 ps, 13.7%, and 3.1/2.2 mm using FBP/OSEM respectively. Then, we demonstrated the benefits of the fine-time performance of the prototype scanner in several different known ways. We observed considerable improvements in the image quality (i.e., better BVs while maintaining the CRCs in the IEC body phantom image) by employing 360 ps TOF information in the reconstruction. The significant positive impact of the fine-time performance and high spatial resolution was obvious in PET images generated using inconsistent physical correction factors, incompletely sampled data, and joint estimation algorithms (i.e., less artifacts and better accuracy). It is noteworthy that the limited axial coverage (i.e., 4.64 cm) of the scanner contributed to high spatial resolution, because only marginally oblique lines of response (maximum degree of 3.75°) were included to measure the resolution using 2D FBP.

The intrinsic performance of the system was slightly degraded compared to the previous study,³⁰ which measured

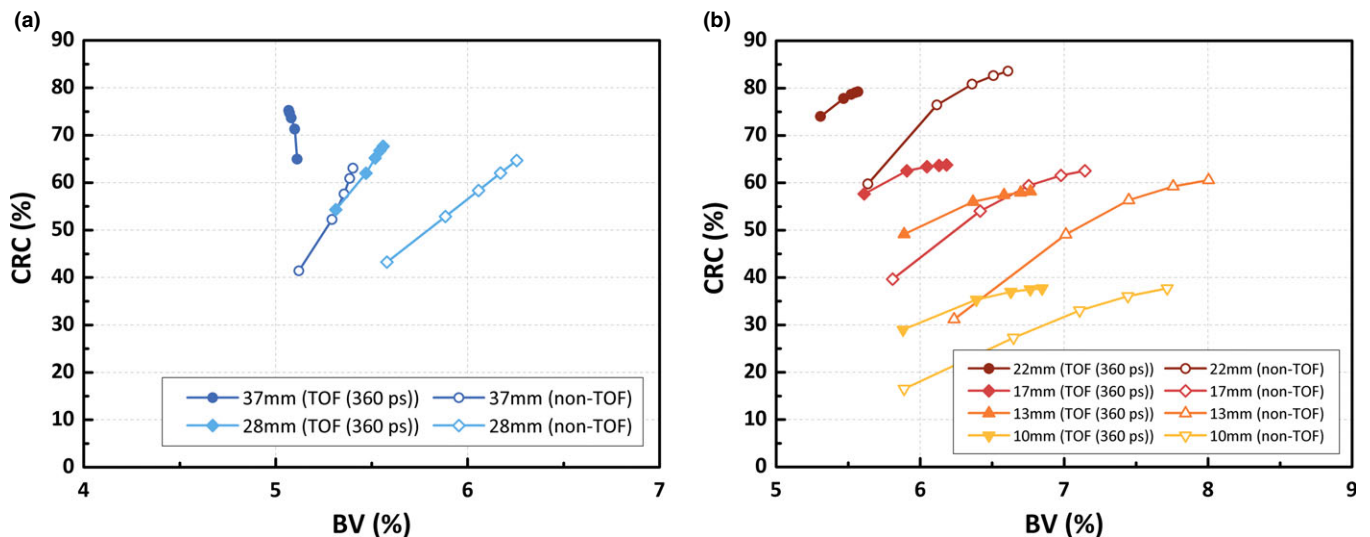


FIG. 6. CRC vs. BV with different numbers of iterations (1, 2, 3, 4, and 5) for (a) cold lesions (spheres 28 and 37 mm in diameter) and (b) hot lesions (spheres 10, 13, 17, and 22 mm in diameter). [Color figure can be viewed at wileyonlinelibrary.com]

the average performance of forty detectors—DWR 5.3 vs. 3.8, energy resolution 11.0% vs. 13.7% and coincidence resolving time 341 ps vs. 360 ps. There are two main reasons for the degradation: the inclusion of multiplexing circuit²⁷ and reduced coupling efficiency between scintillators and PMTs. Because position-encoding signals were multiplexed, the gain of the signals were reduced and crystal identification and energy performance was degraded. The coupling efficiency was reduced as optical grease used for coupling crystal blocks and PMTs got aged, leading to the intrinsic performance degradation.

The average energy resolution (i.e., 13.7%) of the developed scanner is comparable to those of current PMT-based clinical PET scanners (i.e., 11.5–13.7%) despite of the smaller crystal dimension. The coincidence resolving time (i.e.,

360 ps) and spatial resolution (i.e., 3.5 mm) are also better than those of the systems (i.e., 450–544 ps and 4.4–5.1 mm).^{10,11,38} Compared with single-channel PMT-based PET scanners with similar timing resolutions (i.e., 314 ps²⁰ and 375 ps²¹), spatial resolution of our scanner is better than those of the scanners (i.e., 5.1 mm and 5.8 mm, respectively) because of larger number of PMT channels used to read scintillators and smaller gap size between each PMT.

As the benefits of TOF reconstruction were verified using the prototype scanner, the developed PET system can serve as a demonstrator that provides experimental evidence of the impact of the fine-time performance of PET scanners. In particular, it will be useful for verifying the feasibility of new PET applications, which has been traditionally difficult because of the limitations of low true counts^{39–41} and large

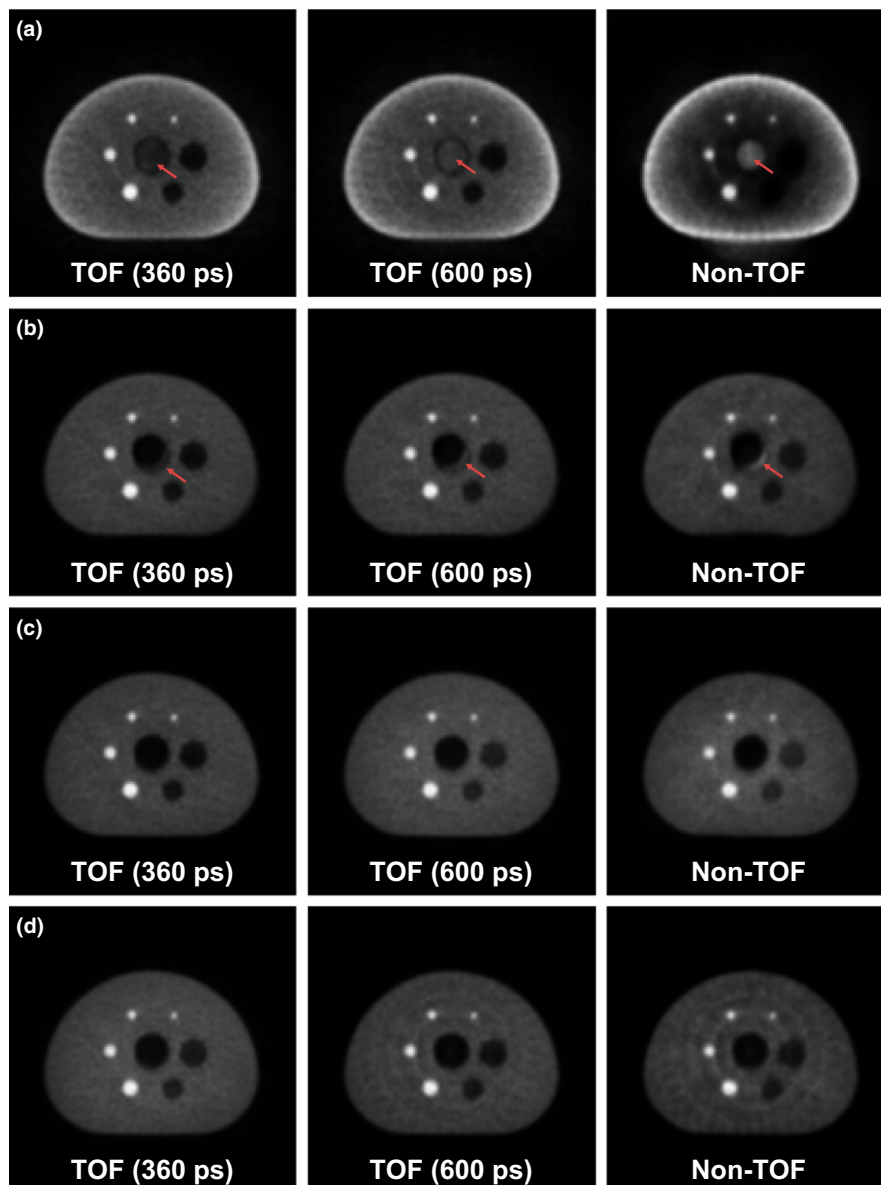


FIG. 7. Phantom images reconstructed without applying one of correction factors: (a) without attenuation correction, (b) with attenuation map mismatch, (c) without scatter correction, and (d) without normalization. [Color figure can be viewed at wileyonlinelibrary.com]

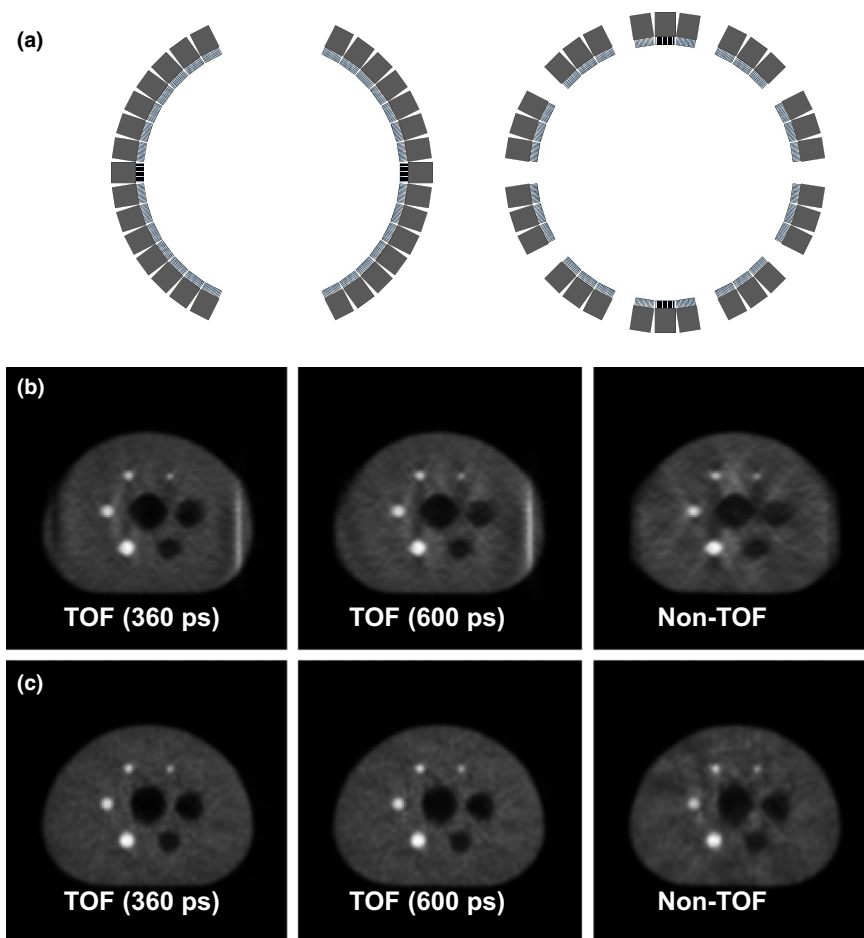


FIG. 8. (a) Partial ring geometries (left: split-ring, right: sparse-ring) and reconstructed phantom images using (b) split-ring geometry, and (c) sparse-ring geometry. [Color figure can be viewed at wileyonlinelibrary.com]

image distortion.^{6,7,34} In addition, the scanner will be useful for facilitating research on the mechanisms of TOF PET techniques and improving advanced PET reconstruction algorithms, e.g., convergence acceleration and crosstalk reduction in joint activity and attenuation estimation⁴² and gap artifact reduction in sparse PET by combining the TOF and compressed-sensing techniques.⁴³

The timing resolution of the multianode PMT-based PET scanner can be enhanced by utilizing the state-of-the-art features of advanced scintillators and multianode PMTs. Fast versions of LGSOs (0.025%Ce) and Ca-codoped LSOs (0.4%Ca) are good candidates for alternative scintillators because of their bright light output (i.e., above 30 k photons/MeV)^{44,45} and fast decay time (~ 30 ns),¹⁵ which have led to coincidence resolving times of 120 and 140 ps with $2.9 \times 2.9 \times 20$ and $2 \times 2 \times 20$ mm³ crystals respectively.^{15,46} Additionally, crystals generating prompt photons such as CdSe nanoplates⁴⁷ and ZnO:Ga nanocrystals⁴⁸ have the potential to achieve a better timing resolution because of their significantly faster emission rate compared with conventional scintillation mechanisms.⁴⁹ Applying nanostructures on the exit surface (i.e., photonic crystal) can allow the extraction of additional photons, leading to improved photo-statistics and an enhanced timing performance, as well as

increased early-phase photons.⁵⁰ Regarding multianode PMTs, employing photocathodes with a higher QE (i.e., ultra-bialkali) results in a better timing resolution.²⁴ Furthermore, because the single-photon optimized dynode structure can separate single photon from the noise,⁵¹ multianode PMTs equipped with this dynode structure has the potential to resolve a single prompt photon described earlier.^{47,48}

The limitation of the prototype scanner presented in this study is the long acquisition time required to obtain a sufficient number of coincidence events as inferred from the sensitivity results, which is mainly due to the short axial coverage of the scanner. Count rate performance of the scanner was limited due to not only insufficient sensitivity, but also the usage of multiplexers. Extending axial coverage of the PET scanner achieved by adding additional detector rings as well as removing multiplexers will yield an improved sensitivity and count rate performance.

5. CONCLUSION

We developed a prototype TOF PET scanner based on an advanced high-QE multianode PMT and demonstrated the benefits of its fine-time performance by conducting phantom studies. The results suggest that the prototype scanner can

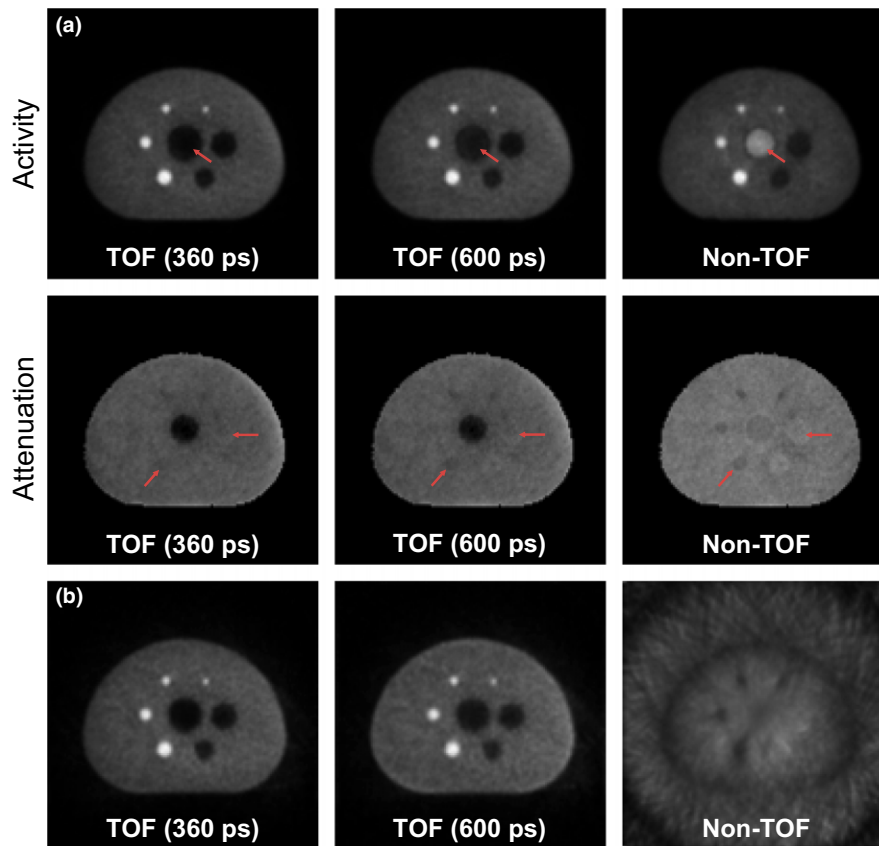


FIG. 9. (a) Reconstructed activity (top) and attenuation (bottom) images obtained by applying the MLAA algorithm and (b) reconstructed activity images obtained using the MLACF algorithm. [Color figure can be viewed at wileyonlinelibrary.com]

serve as an experimental validator of the TOF gains and can be utilized to investigate new applications of PET scans as well as to deeply understand TOF techniques. The limitation of the short axial coverage of the scanner can be overcome by using additional detector rings.

ACKNOWLEDGMENT

This work was supported by grants from the National Research Foundation of Korea (NRF) funded by the Korean Ministry of Science, ICT and Future Planning (grant no. NRF-2014M3C7034000 and NRF-2016R1A2B3014645).

CONFLICT OF INTEREST

None of the authors has any conflict of interest, financial or otherwise, that may directly or indirectly influence the content of the manuscript submitted.

^{a)} Author to whom correspondence should be addressed. Electronic mail: jaes@snu.ac.kr; Telephone: 82-2-2072-2938.

REFERENCES

- Moses WW. Time of flight in PET revisited. *IEEE Trans Nucl Sci.* 2003;50:1325–1330.
- Karp JS, Surti S, Daube-Witherspoon ME, Muehllehner G. Benefit of time-of-flight in PET: experimental and clinical results. *J Nucl Med.* 2008;49:462–470.
- Kadrmas DJ, Casey ME, Conti M, Jakoby BW, Lois C, Townsend DW. Impact of time-of-flight on PET tumor detection. *J Nucl Med.* 2009;50:1315–1323.
- Lois C, Jakoby BW, Long MJ, et al. An assessment of the impact of incorporating time-of-flight information into clinical PET/CT imaging. *J Nucl Med.* 2010;51:237–245.
- Conti M. Why is TOF PET reconstruction a more robust method in the presence of inconsistent data? *Phys Med Biol.* 2011;56:155–168.
- Surti S, Zou W, Daube-Witherspoon ME, McDonough J, Karp JS. Design study of an *in situ* PET scanner for use in proton beam therapy. *Phys Med Biol.* 2011;56:2667–2685.
- Lee E, Werner ME, Karp JS, Surti S. Design optimization of a time-of-flight, breast PET scanner. *IEEE Trans Nucl Sci.* 2013;60:1645–1652.
- Rezaei A, Defrise M, Bal G, et al. Simultaneous reconstruction of activity and attenuation in time-of-flight PET. *IEEE Trans Med Imaging.* 2012;31:2224–2233.
- Rezaei A, Defrise M, Nuyts J. ML-reconstruction for TOF-PET with simultaneous estimation of the attenuation factors. *IEEE Trans Med Imaging.* 2014;33:1563–1572.
- Jakoby BW, Bercier Y, Conti M, Casey ME, Bendriem B, Townsend DW. Physical and clinical performance of the mCT time-of-flight PET/CT scanner. *Phys Med Biol.* 2011;56:2375–2389.
- Bettinardi V, Presotto L, Rapisarda E, Picchio M, Gianolli L, Gilardi MC. Physical performance of the new hybrid PET/CT discovery-690. *Med Phys.* 2011;38:5394–5411.
- Wong W-H, Li H, Zhang Y, et al. A high-resolution time-of-flight clinical PET detection system using a gapless PMT-quadrant-sharing method. *IEEE Trans Nucl Sci.* 2015;62:2067–2074.
- Nguyen NC, Vercher-Conejero JL, Sattar A, et al. Image quality and diagnostic performance of a digital PET prototype in patients with

- oncologic diseases: initial experience and comparison with analog PET. *J Nucl Med.* 2015;56:1378–1385.
14. Gundacker S, Acerbi F, Auffray E, et al. State of the art timing in TOF-PET detectors with LuAG, GAGG and L(Y)SO scintillators of various sizes coupled to FBK-SiPMs. *J Instrum.* 2016;11:P08008.
 15. Cates JW, Levin CS. Advances in coincidence time resolution for PET. *Phys Med Biol.* 2016;61:2255–2264.
 16. Yoon HS, Ko GB, Kwon SI, et al. Initial results of simultaneous PET/MRI experiments with an MRI-compatible silicon photomultiplier PET scanner. *J Nucl Med.* 2012;53:608–614.
 17. Ko GB, Yoon HS, Kim KY, et al. Simultaneous multi-parametric PET/MRI with silicon photomultiplier PET and ultra-high field MRI for small animal imaging. *J Nucl Med.* 2016;57:1309–1315.
 18. Levin CS, Maramraju SH, Khalighi MM, Deller TW, Delso G, Jansen F. Design features and mutual compatibility studies of the time-of-flight PET capable GE SIGNA PET/MR system. *IEEE Trans Med Imaging.* 2016;35:1907–1914.
 19. Adamo G, Parisi A, Stivala S, et al. Silicon photomultipliers signal-to-noise ratio in the continuous wave regime. *IEEE J Sel Topics Quantum Electron.* 2014;20:3804907.
 20. Peng Q, Choong W-S, Vu C, et al. Performance of the Tachyon time-of-flight PET camera. *IEEE Trans Nucl Sci.* 2015;62:111–119.
 21. Daube-Witherspoon ME, Surti S, Perkins A, et al. The imaging performance of a LaBr₃-based PET scanner. *Phys Med Biol.* 2010;55:45–64.
 22. Hirano Y, Nitta M, Inadama N, et al. Performance evaluation of a depth-of-interaction detector by use of position-sensitive PMT with a super-bialkali photocathode. *Radiol Phys Technol.* 2014;7:57–66.
 23. Yamamoto S, Watabe H, Kato K, Hatazawa J. Performance comparison of high quantum efficiency and normal quantum efficiency photomultiplier tubes and position sensitive photomultiplier tubes for high resolution PET and SPECT detectors. *Med Phys.* 2012;39:6900–6907.
 24. Ko GB, Lee JS. Performance characterization of high quantum efficiency metal package photomultiplier tubes for time-of-flight and high-resolution PET applications. *Med Phys.* 2015;42:510–520.
 25. Lee CM, Kwon SI, Ko GB, et al. A novel compensation method for the anode gain non-uniformity of multi-anode photomultiplier tubes. *Phys Med Biol.* 2012;57:191–207.
 26. Kwon SI, Lee JS, Yoon HS, et al. Development of position encoding circuit for a multi-anode position sensitive photomultiplier tube. *Nucl Med Mol Imaging.* 2008;42:469–477.
 27. Yoon HS, Lee JS. Bipolar analog signal multiplexing for position-sensitive PET block detectors. *Phys Med Biol.* 2014;59:7835–7846.
 28. Won JY, Kwon SI, Yoon HS, Ko GB, Son J-W, Lee JS. Dual-phase tapped-delay-line time-to-digital converter with on-the-fly calibration implemented in 40 nm FPGA. *IEEE Trans Biomed Circuits Syst.* 2016;10:231–242.
 29. Yoon HS. Network based high performance data acquisition system for PET scanner. Ph. D. dissertation. Dept. Biomed. Sci., Seoul Natl. Univ., Seoul, Korea; 2015.
 30. Son J-W, Ko GB, Won JY, Yoon HS, Lee JS. Development and performance evaluation of a time-of-flight positron emission tomography detector based on a high-quantum-efficiency multi-anode photomultiplier tube. *IEEE Trans Nucl Sci.* 2016;63:44–51.
 31. Son J-W, Lee MS, Lee JS. A depth-of-interaction PET detector using a stair-shaped reflector arrangement and a single-ended scintillation light readout. *Phys Med Biol.* 2017;62:465–483.
 32. NEMA standards publication NU2-2007. *Performance Measurements of Positron Emission Tomographs.* Rosslyn, VA: National Electrical Manufacturers Association; 2007.
 33. Langen KM, Jones DTL. Organ motion and its management. *Int J Rad Oncol Biol Phys.* 2001;50:265–278.
 34. Surti S, Karp JS. Design considerations for a limited angle, dedicated breast TOF PET scanner. *Phys Med Biol.* 2008;53:2911–2921.
 35. Crespo P, Shakirin G, Fiedler F, Enghardt W, Wagner A. Direct time-of-flight for quantitative, real-time in-beam PET: a concept and feasibility study. *Phys Med Biol.* 2007;52:6795–6811.
 36. Tashima H, Yoshida E, Inadama N, et al. Development of a small single-ring OpenPET prototype with a novel transformable architecture. *Phys Med Biol.* 2016;61:1795–1809.
 37. Takuwa H, Ikoma Y, Yoshida E, et al. Development of a simultaneous optical/PET imaging system for awake mice. *Phys Med Biol.* 2016;61:6430–6440.
 38. Burr KC, Wang G-CJ, Mann G, et al. A new modular and scalable detector for a time-of-flight PET scanner. in *IEEE Nucl Sci Symp Med Imaging Conf.*; 2012:2830–2834.
 39. Lhommel R, Goffette P, den Eynde MV, et al. Yttrium-90 TOF PET scan demonstrates high-resolution biodistribution after liver SIRT. *Eur J Nucl Med Mol Imaging.* 2009;36:1696.
 40. Wright BD, Lapi SE. Designing the magic bullet? The advancement of immuno-PET into clinical use. *J Nucl Med.* 2013;54:1171–1174.
 41. Kurz C, Bauer J, Conti M, Guérin L, Eriksson L, Parodi K. Investigating the limits of PET/CT imaging at very low true count rates and high random fractions in ion-beam therapy monitoring. *Med Phys.* 2015;42:3979–3991.
 42. Chun SY, Kim KY, Lee JS, Fessler JA. Joint estimation of activity distribution and attenuation map for TOF-PET using alternating direction method of multiplier. in *IEEE Int Symp Biomed Imaging*; 2016:86–89.
 43. Ahn S, Kim SM, Son J, Lee DS, Lee JS. Gap compensation during PET image reconstruction by constrained, total variation minimization. *Med Phys.* 2012;39:589–602.
 44. Spurrier MA, Szupryczynski P, Yang K, Carey AA, Melcher CL. Effect of Ca²⁺ co-doping on the scintillation properties of LSO:Ce. *IEEE Trans Nucl Sci.* 2008;55:1178–1182.
 45. Loignon-Houle F, Pepin CM, Lecomte R. Scintillation characteristics of 90%Lu LGSO with different decay times. in *IEEE Nucl Sci Symp Med Imaging Conf*; 2014:1–3.
 46. Nemallapudi MV, Gundacker S, Lecoq P, et al. Sub-100 ps coincidence time resolution for positron emission tomography with LSO: Ce codoped with Ca. *Phys Med Biol.* 2015;60:4635–4649.
 47. Turtos RM, Gundacker S, Polovitsyn A, et al. Ultrafast emission from colloidal nanocrystals under pulsed X-ray excitation. *J Instrum.* 2016;11:P10015.
 48. Turtos RM, Gundacker S, Lucchini MT, et al. Timing performance of ZnO: Ga nanopowder composite scintillators. *Phys Status Solidi RRL.* 2016;10:843–847.
 49. Lecoq P, Auffray E, Gundacker S, Turtos RM. The route to 10 ps TOF-PET is open. in *IEEE Nucl Sci Symp Med Imaging Conf*; 2016.
 50. Lecoq P, Auffray E, Knapitsch A. How photonic crystals can improve the timing resolution of scintillators. *IEEE Trans Nucl Sci.* 2013;60:1653–1657.
 51. Adamczewski-Musch J, Akishin P, Becker K-H, et al. Single photon test bench for series tests of HAMAMATSU H12700 MAPMTs. *Nucl Instrum Methods Phys Res A.* 2017. In Press. <https://doi.org/10.1016/j.nima.2017.02.034>